Sequential {1012} twinning stimulated by other twins in titanium

Article *in* Acta Materialia · April 2017
DOI: 10.1016/j.actamat.2017.04.023

6 authors, including:

Shun Xu
University of Nebraska at Lincoln
16 PUBLICATIONS **102** CITATIONS
SEE PROFILE

Mingyu Gong
University of Nebraska at Lincoln
6 PUBLICATIONS **22** CITATIONS
SEE PROFILE

Christophe Schuman
University of Lorraine
40 PUBLICATIONS **216** CITATIONS
SEE PROFILE

Jean-Sebastien Lecomte
University of Lorraine
75 PUBLICATIONS **536** CITATIONS
SEE PROFILE

Acta Materialia 132 (2017) 57–68

Contents lists available at ScienceDirect

Acta Materialia

journal homepage: www.elsevier.com/locate/actamat

Full length article

Sequential $\{10\bar{1}2\}$ twinning stimulated by other twins in titanium

Shun Xu [a, b, c], Mingyu Gong [c], Christophe Schuman [a, b, **], Jean-Sébastien Lecomte [a, b], Xinyan Xie [c], Jian Wang [c, *]

[a] Laboratoire d'Etude des Microstructures et de Mécanique des Matériaux (LEM3), CNRS UMR 7239, Université de Lorraine, F-57045, Metz, France
[b] Laboratory of Excellence on Design of Alloy Metals for low-mAss Structures (DAMAS), Université de Lorraine, France
[c] Mechanical and Materials Engineering, University of Nebraska-Lincoln, Lincoln, NE 68588, USA

ARTICLE INFO

Article history:
Received 29 December 2016
Received in revised form
7 April 2017
Accepted 9 April 2017
Available online 18 April 2017

Keywords:
Titanium
Twinning
Variant selection
Twin-twin junction

ABSTRACT

We experimentally studied sequential $\{10\bar{1}2\}$ twinning in rolled pure titanium at room temperature and identified a new sequential twinning mechanism, i.e., $\{10\bar{1}2\}$ (T_i^I) extension twin stimulated by the twin-twin junction of two primary $\{11\bar{2}1\}$ extension twins T_{i-1}^{II} and T_i^{II}, which holds a certain relation $T_{i-1}^{II}T_i^{II} \rightarrow T_i^I$. Schmid factor analysis, as the local stress is taken into account, is able to determine the position of sequential twin variant, but cannot determine the twin variant. Displacement gradient accommodation is used to determine the twin variant. The well-known secondary $\{10\bar{1}2\}$ (T_j^I) extension twins in primary $\{11\bar{2}2\}$ (C_i^I) contraction twins (referred to as $C_i^I \rightarrow T_j^I$ double twinning) are also analyzed according to a generalized Schmid factor analysis. Displacement gradient accommodation and twin nucleation based on dislocations dissociation only work well for the most active twin variants, but cannot address other phenomena associated with $C_i^I \rightarrow T_j^I$ double twinning. For rarely activated twin variants, displacement gradient accommodation was not satisfied.

1. Introduction

Titanium with hexagonal close packed structure (referred to as α-Ti) is used in different industries [1–4]. α-Ti plastically deforms via slips and twins. A tremendous amount of experimental work has been carried out for α-Ti and other hexagonal metals to understand mechanisms and mechanics of slips and twins in the context of temperatures and strain rates [5,6], cyclic loading [7–9], strain path changes [10], textures [11,12], twinning modes [13], grain size effects [14,15], and sample size effects [16]. In addition to slips associated with basal <***a***> slips $\{0002\}11\bar{2}0$, prismatic <***a***> slips $\{1\bar{1}00\}11\bar{2}0$, pyramidal <***c***+***a***> slips $\{10\bar{1}1\}11\bar{2}\bar{3}$, and pyramidal <***a***> slips $\{1\bar{1}01\}11\bar{2}0$ at room temperature [17,18], twinning is a prevalent deformation mechanism to accommodate imposed strains. $\{10\bar{1}2\}\bar{1}011$ extension twinning and $\{11\bar{2}2\}11\bar{2}\bar{3}$ contraction twinning were most commonly observed at room temperature [19,20]. Other twinning modes, $\{11\bar{2}1\}\bar{1}126$ extension twinning [21–24], $\{11\bar{2}4\}22\bar{4}\bar{3}$ contraction twinning, and $\{10\bar{1}1\}10\bar{1}\bar{2}$ contraction twining [25,26], occur depending on temperature and loading condition. Extension twinning relates to the aspect of introducing a positive strain along the *c*-axis of the parent grain and contraction refers to a negative component along the *c*-axis. Twinning in hexagonal materials is directional with a unique sense of shear and occurs at low shear stress [27]. A localized shear deformation associated with twinning results in mechanical instability of hexagonal metals [28,29]. As a consequence of the polarity of twinning, rolled hexagonal metal plates exhibit a characteristic texture [30]; the flow stress evolution shows a strong anisotropy between the in-plane and through-thickness directions [31,32]; and aggregated twinning shows an increase in hardening rate and a continuous evolution of grain microstructure with deformation [33,34]. In particular, during cyclic loading or strain-path changes, a twin interacts with another twin, resulting in the formation of twin-twin junctions that influence subsequent plastic deformation modes, slips, twinning, secondary twinning, and de-twinning [35–38]. Thus, there is also an urgent demand for the development of predictive capabilities that can describe twinning and twinning-induced sequential events, and their correlations with microstructures, temperatures, and loading conditions [5,6]. These predictive models will enable engineers to optimize mechanical forming processes of hexagonal metals for specific

* Corresponding author.
** Corresponding author. Laboratoire d'Etude des Microstructures et de Mécanique des Matériaux (LEM3), CNRS UMR 7239,Université de Lorraine, F-57045, Metz, France.
E-mail addresses: christophe.schuman@univ-lorraine.fr (C. Schuman), jianwang@unl.edu (J. Wang).

http://dx.doi.org/10.1016/j.actamat.2017.04.023
1359-6454/

applications [39–42].

The core issues in developing physics-based predictive model include where a twin is initiated, how a certain twin variant is selected, and when twinning occurs [43–47]. According to the sequence of nucleating twin variants in a grain during mechanical loading, deformation twins can be classified into primary twins, secondary twins, and tertiary twins. Corresponding to the statistical nature of twin nucleation, nucleation occurs when the local resolved shear stress on a given twin variant exceeds the statistically assigned nucleation threshold stress [48]. Schmid factor (SF) was extensively used to determine the selection of primary twin variants with the assumption that the local stress is the same as the applied one [49]. However, the local stresses indeed differ from the applied one [50]. This is consistent with the phenomena that twinning is associated with negative SFs in experiments [51,52]. To consider the influence of local stresses on twin nucleation, a random stress that is related to grain orientation, grain size and grain boundaries, is recently added to the applied one [53–55]. Slightly differing from primary twinning, secondary twinning exhibits a strong correlation between the secondary twin variant and primary twins. Several deterministic criteria for the selection of twin variants have been proposed for some specific circumstances, for example, slip transmission induced twin variant [56–58] and twin transmission induced twin variant [25,59–61] across grain boundaries. Correspondingly, the SF criterion was completed with the displacement gradient accommodation (DGA) [51,62], the deformation energy [63], and the nucleation of twinning dislocations based on dislocation dissociation (NDD) [64]. These criteria have been demonstrated validate in accounting for secondary $\{10\bar{1}2\}$ twins in $\{10\bar{1}1\}$ primary twins in Mg [65–68], secondary $\{10\bar{1}2\}$ twins in primary $\{10\bar{1}2\}$ twins [69–71], $\{10\bar{1}2\}$ twinning inside $\{11\bar{2}2\}$ primary twins in α-Ti and Zr [72–75], and secondary twinning or re-twinning during de-twinning as primary twin-twin junction is subjected to reversal loading in Mg [38].

In this paper, we experimentally studied sequential $\{10\bar{1}2\}$ twinning in rolled pure titanium at room temperature. In addition to the well-known secondary $\{10\bar{1}2\}$ extension twins in primary $\{11\bar{2}2\}$ contraction twins (referred to as $\{11\bar{2}2\}\rightarrow\{10\bar{1}2\}$ double twinning), we found a new sequential $\{10\bar{1}2\}$ extension twin that was stimulated by the primary $\{11\bar{2}1\}$ twin-twin junction (referred to as $\{11\bar{2}1\}$ TT Junction$\rightarrow\{10\bar{1}2\}$). We examined the correlation between sequential $\{10\bar{1}2\}$ twin and primary twins, and found that the selection of sequential twin variant can be predicted by the combination of the three criteria — Schmid factor (SF), displacement gradient accommodation (DGA), and the nucleation of twinning dislocations based on dislocation dissociation (NDD). These sequential twinning mechanisms could be implemented into meso- and macro- scale predictive models [34].

2. Experiments

The rolled commercially pure titanium T40 sheet (ASTM grade 2) with the thickness of 1.5 mm was annealed in a vacuum furnace at 800 °C for 3 h. After annealing, the sheet was fully recrystallized with an average grain size of ~200 μm and no twins appear. The annealed sheet was subjected to a compressive strain of 7% at a strain rate 1.0E-3 s^{-1} at room temperature using a Zwick 120T machine. The compression direction is along the ND. After the compression, the surface of the deformed sample was ground with SiC papers of grits from $1200^{\#}$ to $4000^{\#}$. Electrolytic polishing was performed using a solution of 10% perchloric acid and 90% methanol at 35 V for 5 s at 5 °C for EBSD measurements, which were applied on a JEOL JSM-6500F field emission gun scanning electron microscopy (SEM) equipped with an EBSD camera and the AZtec acquisition software package (Oxford Instruments). During that, the sample was tilt by an angle of 70° and a voltage of 15 kV was used. The EBSD patterns for the detailed information on twins were acquired at a step size of 0.2 μm. The data that indicates next-neighbor grain to grain misorientation was processed by using ATOM software [76].

Fig. 1a shows EBSD patterns of the polished surface with a step size of 0.5 μm. Fig. 1b shows twin boundaries that are characterized with a tolerance of ±5° deviation from the ideal crystallographic axis and angle. Corresponding to the crystallography of twins in α-Ti, $\{11\bar{2}1\}$ twinning rotates the twinned domain by ~35° around a $<1\bar{1}00>$ axis; $\{10\bar{1}2\}$ twinning rotates the twinned domain by ~87° around a $<1\bar{2}10>$ axis; $\{11\bar{2}2\}$ twinning rotates the twinned domain by ~64° around a $<1\bar{1}00>$ axis; $\{11\bar{2}4\}$ twinning rotates the twinned domain by ~77° around a $<1\bar{1}00>$ axis, with respect to the parent. We statistically analyzed the next-neighbor grain to grain misorientation (Fig. 1c). The peaks at ~35° and ~64° are attributed to the formation of $\{11\bar{2}1\}$ and $\{11\bar{2}\ 2\}$ twins, respectively. The $\{11\bar{2}4\}$ contraction twins do not produce an obvious peak at ~77° due to their small volume fraction. The maximum peak at ~87° is associated with $\{10\bar{1}2\}$ extension twins. $\{10\bar{1}2\}$ twins are activated either as primary twin in grain (G1 in Fig. 1b) or as secondary twin associated with $\{11\bar{2}2\}\rightarrow\{10\bar{1}2\}$ double twinning (G2 in Fig. 1b) and $\{11\bar{2}1\}$ TT Junction$\rightarrow\{10\bar{1}2\}$ twinning (G3 in Fig. 1b and d). $\{11\bar{2}2\}$ contraction twins are either only one twin variant in grains (G4 in Fig. 1b) or coexistent with secondary $\{10\bar{1}2\}$ extension twin (G2 in Fig. 1b). $\{11\bar{2}1\}$ extension twins in grains are either as single twin variant (G5 in Fig. 1b), coexistent with $\{10\bar{1}2\}$ extension twin (G6 in Fig. 1b) or associated with two variants interaction (G3 in Fig. 1b). The interesting finding is that the interaction between two $\{11\bar{2}1\}$ extension twin variants stimulates $\{10\bar{1}2\}$ twins.

In what follows, we identify secondary $\{10\bar{1}2\}$ twins in EBSD patterns according to the crystallography of twins and then analyze the selection of secondary $\{10\bar{1}2\}$ twin variant according to Schmid factor (SF), displacement gradient accommodation, twin nucleation, and the local stress associated with twin-twin interactions.

3. $\{11\bar{2}1\}$ TT Junction$\rightarrow\{10\bar{1}2\}$ twinning

3.1. Crystallographic character

In hexagonal structure, 12 rotational symmetry matrices result in 6 equivalent variants for each twinning system. We denote twin variants in Fig. 2 as T_i^I for six $\{10\bar{1}2\}$ twin variants and T_i^{II} for six $\{11\bar{2}1\}$ twin variants where i = 1 … 6. The subscript *i* increases by a counter-clockwise rotation around the *c*-axis of the crystal. The zone axis $10\bar{1}0$ associated with a T_i^{II} twin variant is the vector summation of two zone axes $\frac{1}{3}11\bar{2}0$ associated with T_i^I and T_{i+1}^I twins. The red and blue arrows indicate the twinning directions of the two twins.

To characterize the $\{10\bar{1}2\}$ twin variant stimulated by $\{11\bar{2}1\}$ TT junction, the EBSD patterns in Fig. 3a and b were acquired at a step size of 0.2 μm. In order to identify the twin variants, six $\{11\bar{2}1\}$ planes in the matrix and in the twin are plotted into the pole figure corresponding to the orientation of the observed grain (Fig. 3c). The misorientation angle between $(11\bar{2}1)$ plane in T_1^{II} twin and in the matrix is 1.05°, and the misorientation angle between $(\bar{1}2\bar{1}1)$ plane in T_2^{II} twin and the matrix is 2.06°. Thus the two primary twin variants are $(\bar{1}2\bar{1}1)[1\bar{2}16]$ (T_1^{II}) and $(11\bar{2}1)[\bar{1}\bar{1}26]$ (T_2^{II}). Dashed lines in Fig. 3c mark the traces of the two twin planes. The sequential extension twin variant is determined according to the pole figures of $\{10\bar{1}2\}$ planes and of $0\bar{1}11$ twinning directions. The misorientation angle between $(01\bar{1}2)$ planes in the twin and in the matrix is 0.23°, and between $(0\bar{1}12)$ twin planes in the twin and in the matrix is 10.08°, as shown in Fig. 3d. The misorientation angle between $0\bar{1}11$ directions in the T_2^I twin and the matrix is 1.04°, and

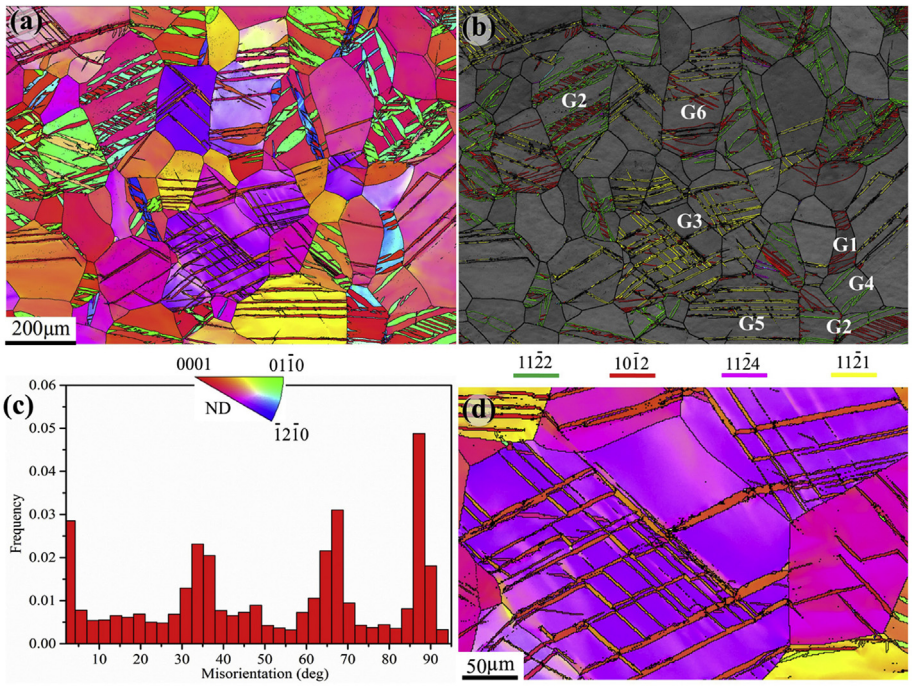

Fig. 1. (a) EBSD patterns of the deformed Ti, (b) the next-neighbor grain to grain misorientation analysis, (c) the distribution of grain misorientation angles, and (d) the magnified EBSD pattern of the region G_3 in (b). The yellow and red lines indicate {11$\bar{2}$1} and {10$\bar{1}$2} twin boundaries; the blue and pink lines indicate {11$\bar{2}$2} and {11$\bar{2}$4} twin boundaries. (For interpretation of the references to colour in this figure legend, the reader is referred to the web version of this article.)

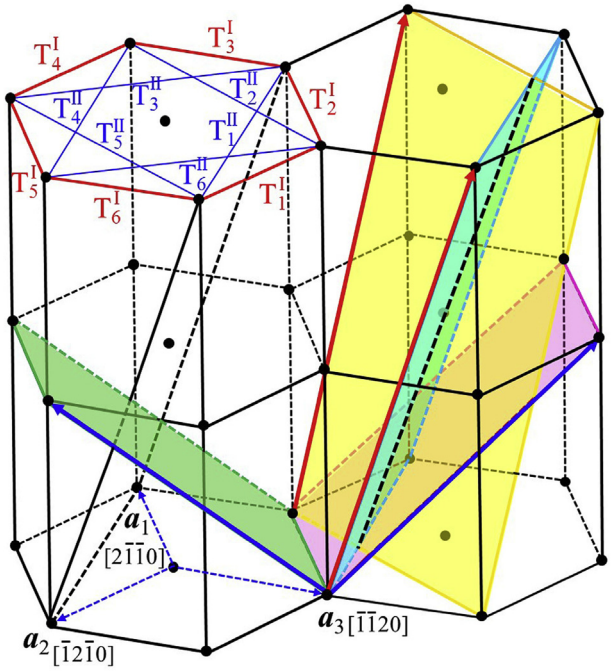

Fig. 2. The crystallography of twins in hexagonal structure. Four shadow planes are twin planes associated with two {11$\bar{2}$1} twins, T_1^{II} (light green) and T_2^{II} (yellow), and two {10$\bar{1}$2} twins T_2^I (pink) and T_5^I (green). Two red arrows indicate the twinning shear directions of {11$\bar{2}$1} twins, and the blue arrows represent the twinning shear directions of {10$\bar{1}$2} twins. (For interpretation of the references to colour in this figure legend, the reader is referred to the web version of this article.)

that between 01$\bar{1}$1 directions in the T_5^I and in matrix is 10.03° as shown in Fig. 3e. According to the crystallography of twins {10$\bar{1}$2} <$\bar{1}$011>, twin variant (01$\bar{1}$2)[0$\bar{1}$11] (T_2^I) is a good fit. The red, green and black dashed lines in Fig. 3a indicate the traces of the three twin planes on the observed surface. The three twins hold a relation of $T_1^{II}T_2^{II} \rightarrow T_2^I$.

There are several geometry features associated with $T_1^{II}T_2^{II} \rightarrow T_2^I$ sequential twinning. The common axis between T_1^{II} and T_2^{II} is parallel to <0$\bar{1}$13> as indicated by a dashed line in Fig. 3f. A twin-twin boundary (TTB) produced by the {11$\bar{2}$1} twin-twin junction is identified to lie in ($\bar{2}$110) plane in the grain (denoted by the while line in Fig. 3f and g) with the assumption that the interface bisects two intersected twinning planes of T_1^{II} and T_2^{II} twins [77]. We conducted statistical analysis in our samples. Among 46 {11$\bar{2}$1} twin-twin junctions, we found that the obvious TTB always forms in the obtuse corner and lie in {$\bar{2}$110} planes. {10$\bar{1}$2} twin variant is also always located at the obtuse region between the two primary twinning planes. We identified 96 {10$\bar{1}$2} twins associated with 46 {11$\bar{2}$1} twin-twin junctions. They hold the relationship that T_i^I forms in the obtuse region between T_{i-1}^{II} and T_i^{II}, where the zone axis associated with T_i^I is a shared vector in describing the zone axis of the two primary twins. Thus such a sequential twinning mechanism can be described by $T_{i-1}^{II}T_i^{II} \rightarrow T_i^I$.

To confirm such a sequential twinning mechanism, we conducted quasi in-situ EBSD analysis by applying two steps of compression along the ND on a pre-polished sample. In the first step, a reduction of 6.2% was applied, followed by EBSD characterization with a step size of 0.2 μm. As shown in Fig. 4a, {11$\bar{2}$1} twin-twin junctions were generated. Then, second step of compression was done with a further reduction of 3.3% along the same direction (ND), followed by EBSD mapping on the same position. Fig. 4b shows that new {10$\bar{1}$2} twins were activated in the obtuse region. In order to identify the twin variants, six {11$\bar{2}$1} planes in the matrix and in the twin are plotted into the pole figure corresponding to the orientation of the observed grain. The misorientation angle between ($\bar{1}\bar{1}$21) plane in T_4^{II} twin and in the matrix is 1.15°, and the misorientation angle between (1$\bar{2}$11) plane in T_5^{II} twin and the matrix is 1.06°. Thus, the two primary twin

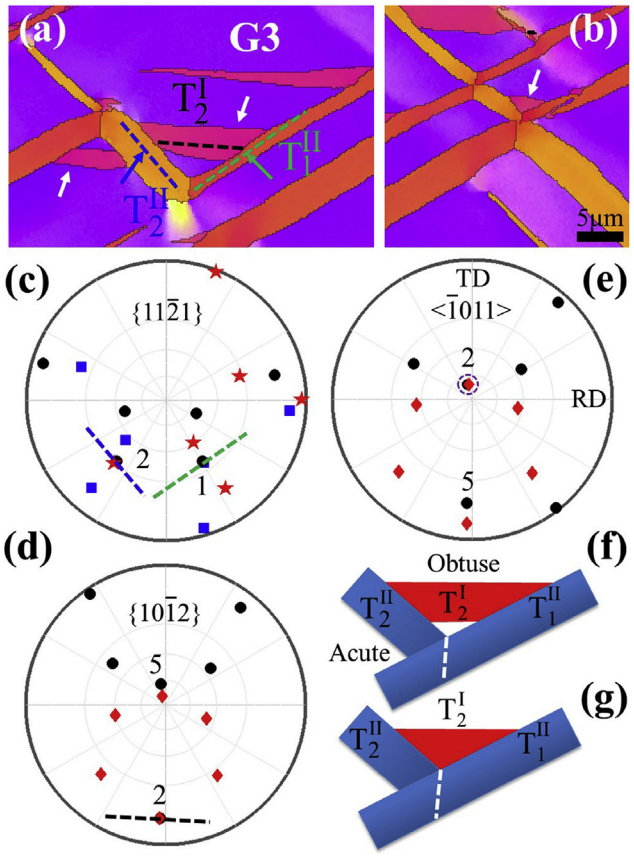

Fig. 3. (a) and (b) EBSD characterization of {10$\bar{1}$2} twins and {11$\bar{2}$1} twin-twin junctions as well as the pole figure of (c) {11$\bar{2}$1} plane, (d) {10$\bar{1}$2} plane, (e) $\bar{1}$011 direction with respect to the orientation of the observed grain. In (c), the black dots represent six {11$\bar{2}$1} twin planes in the matrix, the blue squares and red stars represent six {11$\bar{2}$1} twin variants in two twins. In (d), the black dots represent six {10$\bar{1}$2} twin planes in the matrix, the red diamonds represent six {10$\bar{1}$2} twin planes in the twin, and (e) the black dots represent six $\bar{1}$011 twin directions in the matrix, the red diamonds represent six $\bar{1}$011 twin directions in the twin, (f) and (g) Schematics of {11$\bar{2}$1} TT Junction →{10$\bar{1}$2} sequential twinning. (For interpretation of the references to colour in this figure legend, the reader is referred to the web version of this article.)

variants are ($\bar{1}\bar{1}$21)[11$\bar{2}$6] (T_4^{II}) and (1$\bar{2}$11)[$\bar{1}$2$\bar{1}$6] (T_5^{II}). Dashed lines in Fig. 4c mark the traces of the two twin planes. The sequential {10$\bar{1}$2} extension twin variant is determined according to the pole figures of {10$\bar{1}$2} planes in Fig. 4d and of 0$\bar{1}$11 twinning directions in Fig. 4e. The misorientation angle between (0$\bar{1}$12) planes in the twin and in the matrix is 0.96°, and between (01$\bar{1}$2) twin planes in the twin and in the matrix is 6.16°, as shown in Fig. 4d. The misorientation angle between 01$\bar{1}$1 directions in the T_5^I twin and the matrix is 1.04°, and that between 0$\bar{1}$11 directions in the T_2^I and in matrix is 6.95° as shown in Fig. 4e. According to the crystallography of {10$\bar{1}$2}<$\bar{1}$011> twins, twin variant (0$\bar{1}$12)[01$\bar{1}$1] (T_5^I) is a good fit. The SF of T_4^{II} and T_5^{II} twins in Fig. 4 is 0.424 and 0.369, respectively. They carry the highest and second highest SF among six {11$\bar{2}$1} variants. The SF of active T_5^I and absent T_4^I is 0.277 (the second highest) and 0.345 (highest), respectively. The three twins hold a relation of $T_4^{II}T_5^{II} \rightarrow T_5^I$.

3.2. Selection criteria for $T_{i-1}^{II}T_i^{II} \rightarrow T_i^I$

To understand such a sequential twinning mechanism, we further conduct the analysis of SF, displacement gradient accommodation, and local stress fields, associated with the T_{i-1}^{II} and T_i^{II} junction.

3.2.1. Location selection of sequential twin

Why the sequential twin always presents in the obtuse region is firstly examined according to stress fields due to the two primary twins using finite element method (FEM). In the FEM model shown in Fig. 5a, two {11$\bar{2}$1} twin domains T_1^{II} and T_2^{II} were embedded in a 4040 × 8 matrix through the thickness along the z-axis in the model. In order to conveniently analyze the resolved shear stress on twin planes associated with sequential twinning, the matrix adopts the coordinates with the x-axis along [1$\bar{2}$10], the y-axis normal to ($\bar{3}$032) and the z-axis along [$\bar{1}$01$\bar{3}$]. The z direction is parallel to the intersection line of T_1^{II} and T_2^{II} twin planes. Correspondingly, the trace of the twin plane associated with the sequential twin variant T_2^I or T_5^I is parallel to the x-axis or the y-axis. Two twins have an elliptical shape in the cross-sectional plane along the z-axis. For T_1^{II} twin, the long axis was 22.7 μm and short axis was 3.7 μm. For T_2^{II} twin, the long axis was 15.8 μm and the short axis was 3.1 μm. Anisotropic elastic modulus was assigned into the three regions corresponding to the local orientation [78]. Eigenstrains that mimic the corresponding twinning shear were applied to two twin domains. The model was meshed with 127328 hexahedron elements for better accuracy. To obtain the feature of the elastic stress field, here we conducted linear elastic calculation with free boundaries while ignoring plasticity relaxation associated with slips or twins in the matrix. A thin slice in the middle of the model depicted in Fig. 5a was chosen for the analysis of back-stress that is caused by the two primary twins. Due to the near 90° between the two twin planes associated with twin variants T_2^I and T_5^I, the resolved shear stress associated with T_2^I and T_5^I twins are approximately same. We only show the resolved shear stress field associated with twin variant T_2^I in the matrix in Fig. 5b. Fig. 5c shows the variation of the resolved shear stress along two directions in the acute and obtuse region. The result shows that the resolved shear stress associated with twin variants T_2^I and T_5^I are negative, *i.e.*, opposite to the twin shear direction. However, the resolved shear stress due to the back-stress is smaller in the obtuse region than in the acute region. Under an applied stress, the net resolved shear stress in the obtuse region is thus greater than that in the acute region, favouring sequential extension twinning in the obtuse region. However, the stress analysis could not identify the twin variant between T_2^I and T_5^I.

3.2.2. SF analysis

Corresponding to the crystallography of twins in Fig. 3, SFs associated with T_5^I and T_2^I twins are found to be 0.277 and 0.201, respectively. T_5^I and T_2^I variants carry the highest and second highest SF, but the second high SF twin T_2^I was only activated. It is noticed there is only one specific loading direction along [0$\bar{1}$10] under which T_2^I and T_5^I have the largest and identical SF. There is a question whether the activated twin variant is always associated with the second high SF among six twin variants. Without loss of generality, SF analysis is further conducted under uniaxial compressive stresses that favor two primary twins T_{i-1}^{II} and T_i^{II} among six twin variants. All loading directions that satisfy the condition are grouped into one loading domain (referred to as the $T_{i-1}^{II}T_i^{II}$ loading domain). Fig. 6a shows the $T_{i-1}^{II}T_i^{II}$ loading domain in which the T_1^{II} and T_2^{II} twins are subjected to the highest and secondary higher SF among six {11$\bar{2}$1} twin variants. The red means that both twins have SFs near 0.5, orange and pink mean that the SF of one twin is close to 0.5. We also checked our samples and found that the loadings acting on the grains that have two {11$\bar{2}$1} twin variants are in the loading domain. The black pentagram in Fig. 6a indicates the loading direction of the grain G3 along [0.0501 0.4705–0.5206 -0.3197]. Secondly, we calculate SFs associated with six T_i^I twins as the grain is subjected to uniaxial compression within

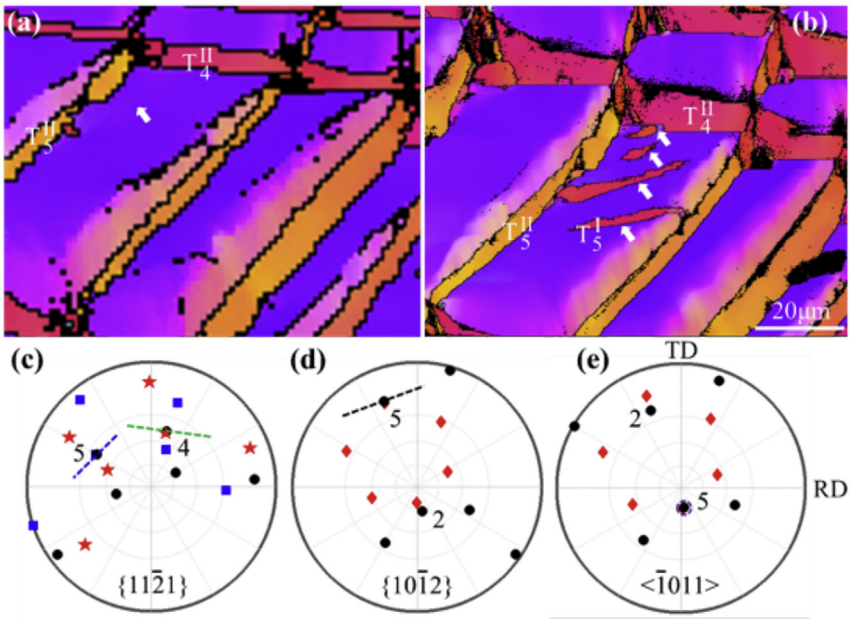

Fig. 4. Quasi in-situ EBSD maps of {11$\bar{2}$1} twin-twin junctions and sequential {10$\bar{1}$2} twins with a reduction of: (a) 6.2%, (b) 9.5% as well as the pole figure of (c) {11$\bar{2}$1} plane, (d) {10$\bar{1}$2} plane, (e) $\bar{1}$011 direction with respect to the orientation of the observed grain. In (c), the black dots represent six {11$\bar{2}$1} twin planes in the matrix, the blue squares and red stars represent six {11$\bar{2}$1} twin variants in two twins. In (d), the black dots represent six {10$\bar{1}$2} twin planes in the matrix, the red diamonds represent six {10$\bar{1}$2} twin planes in the twin, and (e) the black dots represent six $\bar{1}$011 twin directions in the matrix, the red diamonds represent six $\bar{1}$011 twin directions in the twin. (For interpretation of the references to colour in this figure legend, the reader is referred to the web version of this article.)

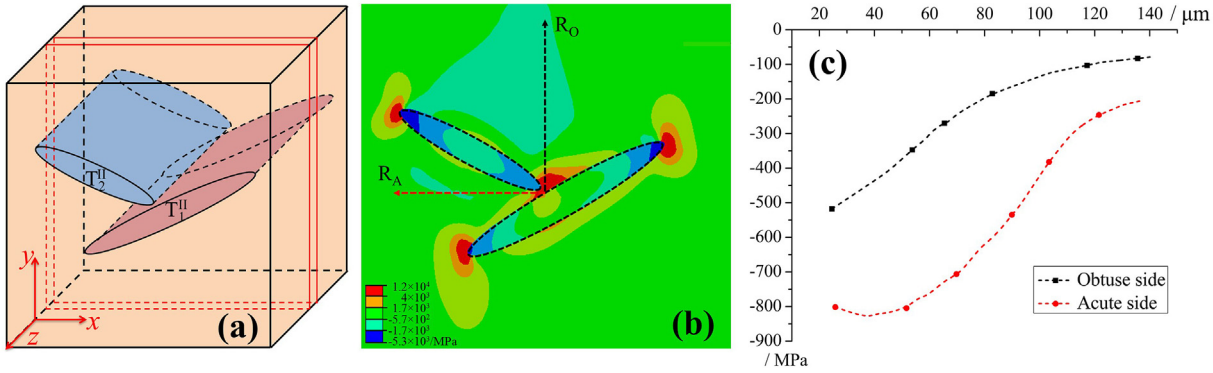

Fig. 5. (a) Schematic of the FEM model. (b) Resolved shear stress fields associated with twin variants T_2^I and T_5^I in the matrix. (c) The variation of the resolved shear stress (MPa, in the vertical axis) along two directions R_o and R_A (μm, in the horizontal axis). The resolved shear stress is caused by the back-stress due to the TT junction.

the loading domain. Due to the approximate 90° between the twin planes of T_i^I and T_{i+3}^I, a pair of T_i^I and T_{i+3}^I is subjected to the same resolved shear stress. Fig. 6b, c and 6d show the SFs associated with T_1^I and T_4^I, T_2^I and T_5^I, and T_3^I and T_6^I, respectively. The blue color represents negative SFs, and red represents positive SFs. The SFs associated with T_2^I and T_5^I are always greater than that for other two pairs, implying that T_2^I and T_5^I are mechanically preferred if sequential twin occurs. However, the result does not determine the preference between the two variants. We further compare the SFs associated with the two twin variants and found that the SF associated with T_5^I is always higher than the SF associated with T_2^I for any applied compression in the loading domain (Table 1). This is contradictory to EBSD analysis where T_2^I always occurs. Therefore, the SF analysis can determine the group of sequential twins, but cannot help determine the sequential twin variant.

3.2.3. Deformation gradient accommodation

The same shear strain may be associated with different crystal rotation that depends on displacement gradients. Corresponding to the simple shear model associated with twinning, we calculate the deformation gradient resulted from T_1^{II} and T_2^{II} twinning. The displacement gradient tensor of a twin has a simple form in the twinning frame, i.e., x || the twinning shear direction ($\boldsymbol{\eta}$), z || the normal of the twin plane ($\boldsymbol{n}$), and y || the zone axis ($\boldsymbol{\lambda} = \boldsymbol{n} \times \boldsymbol{\eta}$) [51]. The displacement gradient tensor can be written as

$$e_{ij} = \begin{bmatrix} 0 & 0 & s \\ 0 & 0 & 0 \\ 0 & 0 & 0 \end{bmatrix} \quad (1)$$

where $s = 0.63$ for {11$\bar{2}$1} twinning (c/a = 1.587) in α-Ti. In order to examine whether the strain induced by the {11$\bar{2}$1} twin can be accommodated by slips and/or other twins in the grain, the displacement gradient tensors of the intersected {11$\bar{2}$1} twins were transformed into the crystal frame of the grain, i.e., x'|| [10$\bar{1}$0], y'|| [$\bar{1}$2$\bar{1}$0], z'|| [0001]. $e_{x'z'}$ and $e_{y'z'}$ represent the accommodation by

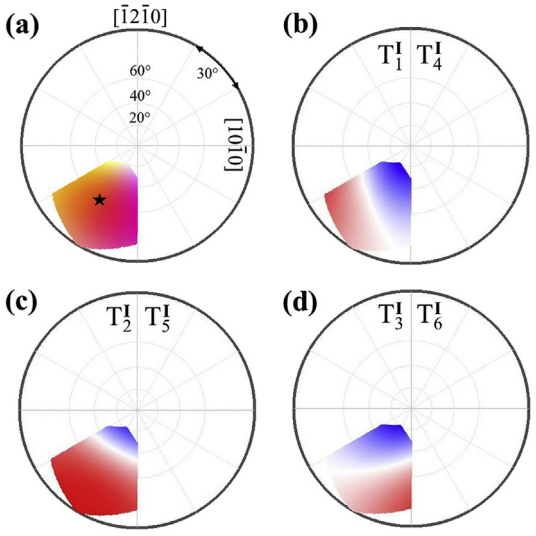

Fig. 6. Inverse pole figures of the Schmid factor of twinning systems subjected to compression: (a) the loading domain in which SFs of T_1^{II} and T_2^{II} twins are positive and are greater than other four equivalent variants. Under this loading domain, the SF associated with sequential twin variants (b) T_1^I and T_4^I, (c) T_2^I and T_5^I, and (d) T_3^I and T_6^I. The blue color represents negative SFs, and red represents positive SFs. (For interpretation of the references to colour in this figure legend, the reader is referred to the web version of this article.)

double and single basal slips, respectively; $e_{z'x'}$ and $e_{z'y'}$ indicate the accommodation by twinning; $e_{x'y'}$ and $e_{y'x'}$ are associated with the accommodation by double and single prismatic slips, respectively [51]. For the two primary twins, the transformed displacement gradient tensors are

$$e_{ij}\left(T_1^{II}\right) = \begin{pmatrix} -0.135 & -0.078 & -0.049 \\ -0.078 & -0.045 & -0.028 \\ 0.496 & 0.287 & 0.181 \end{pmatrix} \quad (2)$$

$$e_{ij}\left(T_2^{II}\right) = \begin{pmatrix} 0 & 0 & 0 \\ 0 & -0.181 & -0.057 \\ 0 & 0.573 & 0.181 \end{pmatrix} \quad (3)$$

$e_{z'x'}$ and $e_{z'y'}$ have big value, implying that dislocation slips could not efficiently accommodate the displacement gradients, instead, extension twinning corresponding to the positive $e_{z'z'}$ could accommodate them.

We thus evaluate the accommodation capacity of six $\{10\bar{1}2\}$ extension twin variants and other four $\{11\bar{2}1\}$ extension twin variants (Table 1). The displacement gradient tensors of the activated $\{11\bar{2}1\}$ twins were transformed into the twinning frames of $\{10\bar{1}2\}$ variants and $\{11\bar{2}1\}$ variants, respectively. As summarized in Table 1, four $\{11\bar{2}1\}$ twin variants do not accommodate the displacement gradient component due to the negative sign. The variant T_2^I has the largest e_{13} among six $\{10\bar{1}2\}$ and four $\{11\bar{2}1\}$ twins, implying that T_2^I twin variant can effectively accommodate the displacement gradient component generated by the two $\{11\bar{2}1\}$ primary twins. T_5^I twin with the highest SF does not accommodate the displacement gradient component because of the negative sign. Other twin variants, T_1^I and T_4^I, can accommodate the displacement gradients, while they often have small SFs, and even negative SFs (Table 1). Thus, the combination of SF and DGA criteria assures the relation of $T_{i-1}^{II}T_i^{II} \rightarrow T_i^I$.

4. $\{11\bar{2}2\} \rightarrow \{10\bar{1}2\}$ double twinning

4.1. Crystallography of $\{11\bar{2}2\} \rightarrow \{10\bar{1}2\}$ double twins

For simplicity in describing twins later, we denote twin variants in Fig. 7 as T_i^I for six $\{10\bar{1}2\}$ twin variants and C_i^I for six $\{11\bar{2}2\}$ twin variants where i = 1, 2, 3 … 6. The subscript i increases by a counterclockwise rotation around the *c*-axis of the crystal. The zone axis $10\bar{1}0$ associated with a C_i^I twin variant is the vector summation of two zone axes $\frac{1}{3}11\bar{2}0$ associated with T_i^I and T_{i+1}^I twins. Comparing the parent grain orientation to secondary twins inside, there are 36 possible combinations. The misorientation between a secondary $\{10\bar{1}2\}$ twin originating from a primary $\{11\bar{2}2\}$ twin and its parent grain was determined by rotating the orientation of the parent grain around the respective normal directions of primary and secondary twinning planes by 180°. Then, the 12 symmetry operations of the hexagonal lattice were applied and the minimum misorientation angle and corresponding axis were computed between the orientation matrix of the parent and the 12 equivalent matrices of the secondary twin. According to misorientation between the matrix and the secondary twins, six $\{10\bar{1}2\}$ secondary twins inside a primary $\{11\bar{2}2\}$ twin were categorized into 3 groups: $C_i^I \rightarrow T_{i+3}^I$ and T_{i+4}^I (Group I), $C_i^I \rightarrow T_i^I$ and T_{i+1}^I (Group II), and $C_i^I \rightarrow T_{i+2}^I$ and T_{i+5}^I (Group III). In Group I, the angle between two twin planes is 95.9° and the angle between two twin shear directions is 76.6°. In Groups II and III, the angle between two twin planes is 27.4° and 66.9°, respectively, and the angle between two twin shear directions is 24.2° and 55.2°, respectively.

The crystallographic feature of $C_i^I \rightarrow T_j^I$ double twins is illustrated in Fig. 8. The blue plane denotes the primary twin C_i^I, and the pink plane represents the secondary twin T_j^I. The white dashed line indicates the intersection, l_{ij}, between the primary twin C_i^I and the secondary twin T_j^I. The intersection lines, l_{14} and l_{15} in Group I are along [8 $\bar{1}0$ 2 3] and [$\bar{1}0$ 8 2 3], respectively. The intersection lines l_{11} and l_{12} in Group II are along [$\bar{4}223$] and [$2\bar{4}23$], respectively. The same intersection lines are identified for l_{13} and l_{16} along [$\bar{4}223$] and [$2\bar{4}23$] in Group III, respectively. The intersection lines in

Table 1
The transformation of displacement gradient tensor of T_1^{II} and T_2^{II} twins into the twinning frame of six $\{10\bar{1}2\}$ extension twin variants and other four $\{11\bar{2}1\}$ extension twin variants in the same grain (Euler angle: $\varphi_1 = 0.7°$, $\Phi = 120.5°$, $\varphi_2 = 35°$) as well as the SFs under macro loading (Exp. SFs) and the SFs under a specific loading along [$0\bar{1}0$] direction (Spe. SFs).

Twin variants	Six $\{10\bar{1}2\}$ variants						Four $\{11\bar{2}1\}$ variants			
	T_1^I	T_2^I	T_3^I	T_4^I	T_5^I	T_6^I	T_3^{II}	T_4^{II}	T_5^{II}	T_6^{II}
	$(10\bar{1}2)\bar{1}011$	$(01\bar{1}2)0\bar{1}11$	$(\bar{1}102)1\bar{1}01$	$(\bar{1}012)10\bar{1}1$	$(0\bar{1}12)01\bar{1}1$	$(1\bar{1}02)\bar{1}101$	$(\bar{2}111)2\bar{1}\bar{1}6$	$(\bar{1}\bar{1}21)11\bar{2}6$	$(1\bar{2}11)\bar{1}2\bar{1}6$	$(2\bar{1}\bar{1}1)\bar{2}116$
Spe. SFs	0.125	**0.498**	0.125	0.125	**0.498**	0.125	0	0.215	0.215	0
Exp. SFs	−0.029	**0.201**	−0.078	0.015	**0.277**	−0.046	−0.103	−0.224	−0.225	−0.041
T_1^{II} $(11\bar{2}1)\bar{1}126$	0.41	**0.41**	0.09	−0.10	−0.10	0.09	−0.20	−0.42	−0.20	0.33
T_2^{II} $(\bar{1}2\bar{1}1)1\bar{2}16$	0.09	**0.41**	0.41	0.09	−0.10	−0.10	0.33	−0.20	−0.42	−0.20

The bold font indicates positive and greater SFs.

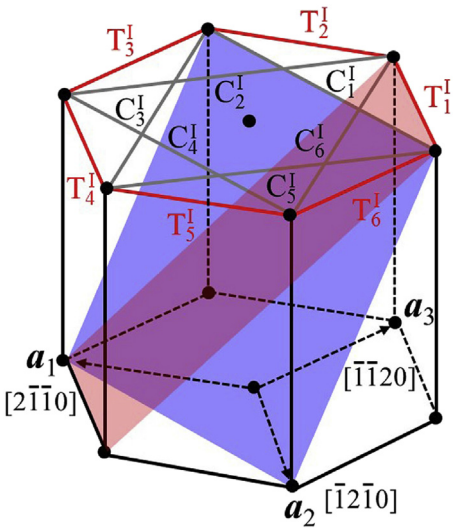

Fig. 7. The crystallography of hexagonal structure. Two shadow planes are twin planes associated with contraction twin $\{11\bar{2}2\}$, C_1^I (blue), and extension twin $\{10\bar{1}2\}$, T_1^I (pink). (For interpretation of the references to colour in this figure legend, the reader is referred to the web version of this article.)

Groups II and III lie in a $\{10\bar{1}0\}$ prismatic plane, as outlined by the yellow dashed lines.

Experiment observations show that Group I, Group II and Group III account for 10.6%, 85.6% and 3.8% of 425 detected $\{11\bar{2}2\}\rightarrow\{10\bar{1}2\}$ double twins [75], respectively. In the previous work [75], the analysis of $\{11\bar{2}2\}\rightarrow\{10\bar{1}2\}$ double twins was applied according to the experimental data. Both intersection lines of the primary and secondary twin planes lie in one active prismatic plane in the primary twin, correspondingly Xu. Et al analyzed the production of twinning partial dislocations. However, this prismatic-dislocation mediated nucleation mechanism is applicable to both Group II and Group III double twin variants, and thus it cannot explain why Group II is preferred over Group III. In this work, we extend the experimental findings to a general case to evaluate whether the prismatic-dislocation mediated nucleation mechanism can distinguish variant selection in all possibilities. Besides, the dissociation of prismatic dislocations into twinning dislocations is applied to both Group II and Group III $\{10\bar{1}2\}$ double twins. Even though the geometrical feature also facilitates the activation of Group III double twins, the dislocation reaction presented in this paper clearly shows that a prismatic dislocation dissociating into three secondary twining dislocations for Group II twin is energetically favored while a prismatic dislocation dissociating into only one twining dislocation associated with Group III twin is energetically unfavorable, which clearly explains why Group III is still difficult to happen. Therefore, only prismatic-dislocation mediated nucleation mechanism can clarify the preference of Group II over Group I and Group III. In addition, with the help of a generalized SF analysis, the stress domains in which only one or two Group II double twin variants can be activated were in agreement with experiments. Therefore, a general and more rigorous prediction of the selection for $\{10\bar{1}2\}$ double twinning variants inside $\{11\bar{2}2\}$ primary twins is presented in this work.

Obviously, Group II twins are predominant among three groups according to statistical analysis. In addition, most primary twins, 95.5% of double twins, contain only one secondary twin variant. Only 4.5% of primary twins in Group II contain two secondary twin variants. In what follows, we tested the variants correlation of $\{11\bar{2}2\}\rightarrow\{10\bar{1}2\}$ double twins according to SF, displacement gradient accommodation, and nucleation of twinning dislocations based on dislocation dissociation.

4.2. Selection criteria for $\{11\bar{2}2\}\rightarrow\{10\bar{1}2\}$ double twins

4.2.1. A generalized SF analysis

Without loss of generality, we conducted a generalized SF analysis. Firstly, we determine the loading domain in which one primary contraction twin is activated. $\{11\bar{2}2\}$ twin variant C_1^I is chosen to be the primary twin in this study. The grain is subjected to uniaxial compression. The loading domain is determined according to the SF associated with C_1^I twin. When the SF is greater than 0.3 and is the greatest among six equivalent variants, the loading directions are plotted into an inverse pole figure as shown in Fig. 9a. Due to the approximate 90° between secondary twin variants T_i^I and T_{i+3}^I, they have nearly same SF. At a given loading direction within the loading domain, we calculated the SFs associated with six $\{10\bar{1}2\}$ twin variants T_j^I ($j = 1 \ldots 6$), and plotted them in Fig. 9b–d. The results show that twin variants T_3^I and T_6^I in Group III have smaller SFs than twin variants in Group II and Group I. The SFs in Group II and I are similar and no significant difference, because T_1^I in Group II has the same SF as T_4^I in Group I, and T_2^I in Group II has the same SF as T_5^I in Group I. This could address the lower activity of twin variants in Group III than other two groups, while this could not distinguish the activity of twin variants in Group II and I. The same feature is associated with other contraction twin variants. For example, the loading domain associated with C_2^I is obtained by counterclockwise rotating the C_1^I loading domain 60° around the <0001>. Three typical loading directions are marked by A, B and C in Fig. 9a. SFs of six secondary twin variants at the three points are given in Table 2. T_1^I and T_4^I have the largest SFs when the loading is along the A; T_2^I and T_5^I have the largest SFs when the loading is along the C. Four variants in Group II and Group I have the largest SFs when the loading is along the B.

We further compared SFs associated with twin variants in Group II. When the difference in the SFs associated with two variants in one group is smaller than 0.05, we treated them equal. Correspondingly, we re-plotted the loading domain in Fig. 9e and f for Group II associated with the primary contraction twin C_5^I and C_4^I, respectively. In a small loading domain (marked by the red color), two variants share the equal SF. In the rest region of the loading domain, one is greater than the other. The same feature is also observed for Group I. This could address why most primary twins only contain one secondary twin variant.

4.2.2. Displacement gradient accommodation

The generalized SF analysis so far well predicts the activity of twin variants in Group II, while the competition of variants between Group II and Group I cannot be accessed. We thus tested displacement gradient accommodation. Displacement gradient tensor of a $(11\bar{2}2)[11\bar{2}3]$ twin expressed in its twinning frame was transformed into the twinning frame of six $\{10\bar{1}2\}$ twins. The component e_{13} is summarized in Table 2. Two variants in Group II have the largest e_{13}, which means that the strain induced by the primary twin can be effectively accommodated by Group II secondary twins. Twin variants in Group I are also observed in experiments, but the displacement gradient tensor is negative. As to twin variants in Group III, the displacement gradient tensor is positive but they are rarely observed in experiments. This implies that displacement gradient accommodation is not the necessity in accessing the variant, but can predict the relative activity when multiple variants have positive SF in the case of $C_i^I\rightarrow T_j^I$ double twins

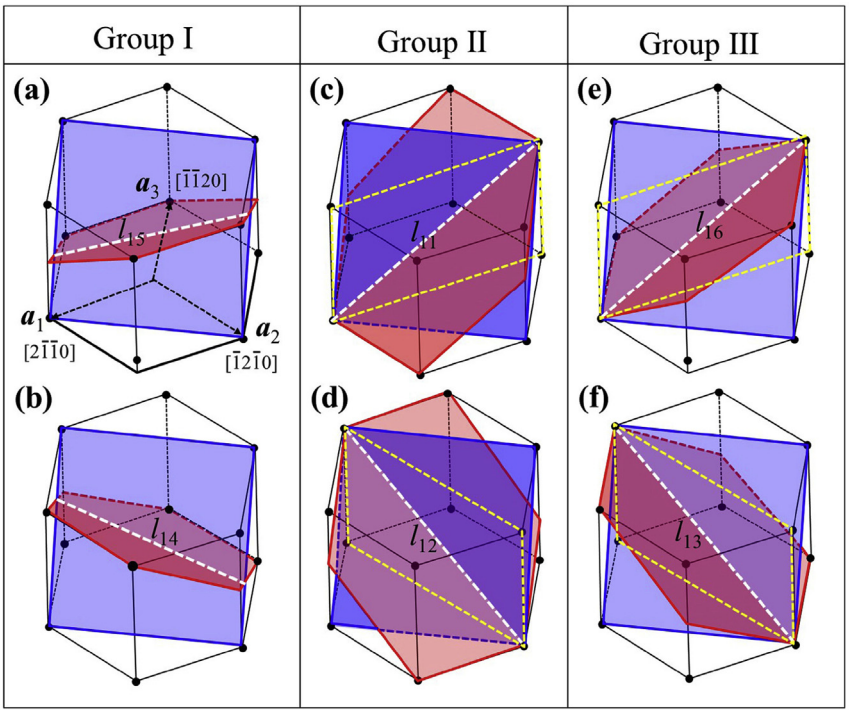

Fig. 8. Crystallography of $\{11\bar{2}2\}\rightarrow\{10\bar{1}2\}$ double twins. The blue plane denotes the primary twin C_i^l, and the pink plane represents the secondary twin T_j^l. The white dashed line indicates the intersection, l_{ij}, between the primary twin C_i^l and the secondary twin T_j^l. The yellow dashed lines outline a $\{10\bar{1}0\}$ prismatic plane. (For interpretation of the references to colour in this figure legend, the reader is referred to the web version of this article.)

(j = i or i+1).

4.2.3. Nucleation based on dislocation dissociation

The selection of secondary twin in the double twinning could be related to twin nucleation at primary twin boundary due to dislocation dissociation. In Mg, $\{10\bar{1}1\}$-$\{10\bar{1}2\}$ were the most commonly observed DTs under uniaxial deformation. In this case, primary and secondary twins have the same axis along *a*-axis. The nucleation of secondary twins inside the contraction twin was proposed by Beyerlein et al. to be aided by the dissociation of basal <***a***> dislocations. In Ti, we examine the dislocation dissociation mechanism associated with prismatic <***a***> dislocations.

The intersection line between two secondary twin variants in Group I and the primary twin $(11\bar{2}2)$ are along $[8\ \bar{1}0\ 2\ 3]$ and $[\bar{1}0\ 8\ 2\ 3]$, respectively. These intersection lines do not lie in any usual slip planes. Thus, dislocation dissociation mechanisms would be difficult unless dislocations can easily climb or cross slip on the twin plane. However, two secondary twin variants in Group II intersect $(11\bar{2}2)$ twin plane along $[\bar{4}223]$ and $[2\bar{4}23]$, respectively. They both lie in a $\{1\bar{1}00\}$ prismatic plane. The same characteristic can be found for two secondary twins variants in Group III. Therefore, nucleation of secondary twin variants in Group II and III could be mediated by the dissociation or reflection of prismatic dislocations.

Taking the similar analysis in Ref. [64], we investigate the dissociation or reflection of prismatic <a> dislocation at the primary twin plane into twinning dislocations associated with $\{10\bar{1}2\}$ twins. As shown in Fig. 10a, secondary T_2^l and T_3^l variants intersect the C_1^l primary twin plane along the $[2\bar{4}23]$ axis, which lies in $(10\bar{1}0)$ prismatic plane. When $(10\bar{1}0)1\bar{2}10$ dislocations approach the primary twin boundary as depicted in Fig. 10b, they could dissociate into twinning dislocations associated with Group II and Group III secondary twins. For Group II, a $(10\bar{1}0)1\bar{2}10$ dislocation, b_a can be dissociated into three secondary twining dislocations $3b_t^{(01\bar{1}2)}$, and a residual one b_r^1,

$$b_a \Rightarrow b_r^1 + 3b_t^{(01\bar{1}2)} \tag{4}$$

according to the Frank's law ($|b_a|^2 > \left|b_r^1\right|^2 + \left|3b_t^{(01\bar{1}2)}\right|^2$). However, a $(10\bar{1}0)1\bar{2}10$ dislocation can dissociate into only one twining dislocation associated with Group III twin,

$$b_a \Rightarrow b_r^2 + b_t^{(1\bar{1}0\bar{2})} \tag{5}$$

The dissociation is energetically unfavorable according to the Frank's law, $|b_a|^2 < \left|b_r^2\right|^2 + \left|b_t^{(1\bar{1}0\bar{2})}\right|^2$. Where $b_a = \frac{1}{3}[1\bar{2}10]$, 0.295 nm for Ti; The magnitude of Burgers vector of $\{10\bar{1}2\}$ twinning dislocation is equal to $\frac{3a^2-c^2}{\sqrt{3a^2+c^2}}$, 0.60 nm for Ti ($a$ = 0.295 nm and c = 0.4683 nm).

If the incoming dislocation b_a is firstly dissociated into twinning dislocation $b_t^{(\bar{1}\bar{1}2\bar{2})}$ on the primary twin plane, and then the residual acts as nucleation source, only one secondary twinning dislocation can be nucleated according to the Frank's law.

$$b_a \Rightarrow b_r^3 + b_t^{(\bar{1}\bar{1}2\bar{2})} + b_t^{(01\bar{1}2)} \tag{6}$$

$$b_a \Rightarrow b_r^4 + b_t^{(\bar{1}\bar{1}2\bar{2})} + b_t^{(1\bar{1}0\bar{2})} \tag{7}$$

Equation (6) was applied for Group II and was energetically favored. Equation (7) was applied for Group III and was energetically unfavorable. The magnitude of Burgers vector of $\{11\bar{2}2\}$ twinning dislocation is equal to $\frac{c^2-2a^2}{\sqrt{c^2+a^2}}$, 0.82 nm for Ti.

The above analysis according to the nucleation of twinning

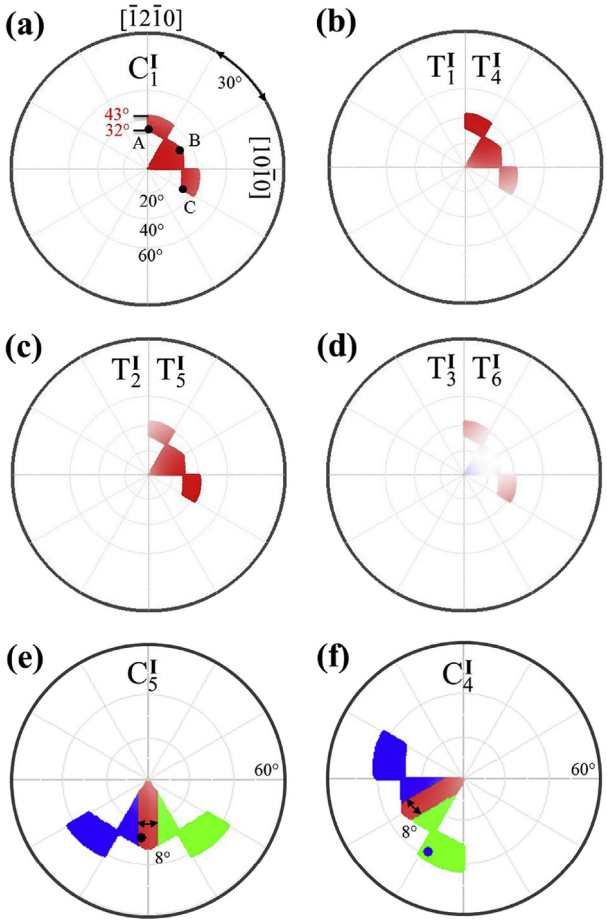

Fig. 9. Inverse pole figures of the Schmid factor of twinning systems subjected to compression: (a) Stress domain where SF of C_1^I primary twin variant is positive and is the largest among the six possibilities. Under this stress domain, the SF of: (b) T_1^I and T_4^I secondary twin variants, (c) T_2^I and T_5^I secondary twin variants, (d) T_3^I and T_6^I secondary twin variants. Distribution of SFs of Group II variants T_i^I and T_{i+1}^I in the loading domain associated with contraction twin (e) C_5^I and (f) C_4^I. Green means the SF associated with variant T_i^I is larger than the variant T_{i+1}^I. Blue means the SF associated with variant T_i^I is smaller than the variant T_{i+1}^I. Red means the difference in the SFs of two variants is less than 0.05. (For interpretation of the references to colour in this figure legend, the reader is referred to the web version of this article.)

dislocations based on the dissociation of prismatic <***a***> dislocation can distinguish the relative activity of three group of twin variants. Group II is predominant, Group III is secondly activate, and Group I

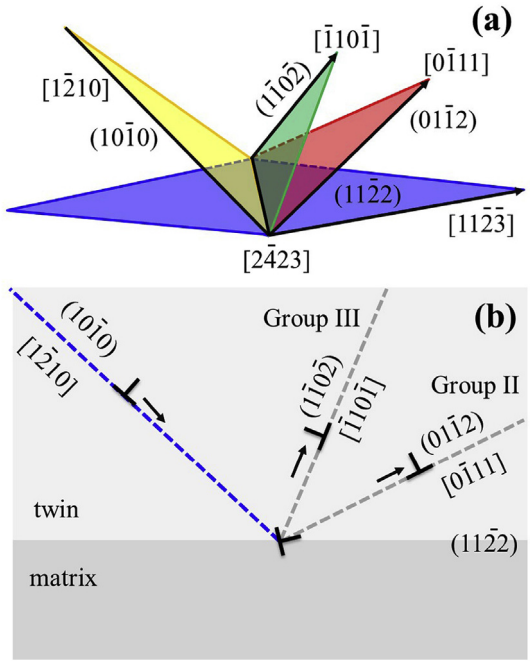

Fig. 10. (a) Illustration of the common line between a prismatic plane, a Group II twinning plane, a Group III twinning plane and a primary twin plane along [$2\bar{4}23$]. (b) Schematic of reaction of a prismatic dislocation at a primary twin boundary into a Group II or a Group III twin dislocation plus a residual dislocation.

is most unlikely. Due to the approximately same resolved shear stress on two twin variants in a group, the nucleation criterion cannot distinguish the preference of two variants in the same group.

5. Discussion

5.1. $T_{i-1}^{II}T_i^{II} \rightarrow T_i^I$ *sequential twinning*

According to EBSD analysis of sequential twins in rolled pure titanium at room temperature, we observed a new sequential twinning mechanism that {10$\bar{1}$2} extension twin is stimulated by the primary {11$\bar{2}$1} twin-twin junction. Among 71 cases of {11$\bar{2}$1} TT Junction→{10$\bar{1}$2} twinning, experimental observations reveal that the relation among three extension twins is $\mathbf{T_{i-1}^{II}T_i^{II} \rightarrow T_i^I}$, and $\mathbf{T_i^I}$ is always formed in the obtuse region between two primary twin planes. Corresponding to the crystallography of twins, six twin

Table 2
Comparison of selection criteria for {11$\bar{2}$2}→{10$\bar{1}$2} double twins. SFs associated with six twin variants correspond to three loading directions A, B and C in Fig. 9a. DGA means displacement gradient accommodation, and NDD represents nucleation based on dislocation dissociation.

In primary twin (C_1^I) [11$\bar{2}$2]11$\bar{2}$3						
Secondary {10$\bar{1}$2} variants	T_4^I ($\bar{1}$012)10$\bar{1}$1	T_5^I (0$\bar{1}$12) 01$\bar{1}$1	T_1^I (10$\bar{1}$2) $\bar{1}$011	T_2^I (01$\bar{1}$2) 0$\bar{1}$11	T_3^I ($\bar{1}$102) 1$\bar{1}$01	T_6^I (1$\bar{1}$02) $\bar{1}$101
Group	I, 41$\bar{5}$3 41.34°		II, 50$\bar{5}$3 48.44°		III, 34$\bar{7}$0 87.85°	
Experiments	10.6%		85.6%		3.8%	
SFs (A)	0.490	0.138	**0.474**	0.129	0.101	0.093
SFs (B)	0.357	0.357	**0.370**	**0.370**	−0.006	−0.006
SFs (C)	0.138	0.490	0.129	**0.474**	0.093	0.101
Generalized SFs	One high, One moderate		One high, One moderate		Two are same and low	
DGA	−0.01	−0.01	**0.18**	**0.18**	0.05	0.05
NDD	Very difficult Unless dislocations climb		Energetically favored by prismatic <***a***> dislocations		Facilitated by prismatic <***a***> dislocations	

The bold font indicates positive and greater SFs.

variants $\mathbf{T_i^I}$ are classified in to 3 groups because of the same SF for a pair of twins $\mathbf{T_i^I}$ and $\mathbf{T_{i+3}^I}$. A generalized SF analysis in the loading domain where the two primary twins are mechanically preferred was performed to select sequential twins. The results show that the SF analysis made the correct choice for group, but wrong for twin variant in the group. Displacement gradient accommodation analysis correctly selected the twin variant in the group which is determined by the SF analysis. When the local stress associated with twin-twin interactions is taken into account for twin nucleation, the location of sequential twin is well predicted in the obtuse region.

5.2. $C_i^I \rightarrow T_j^I$ *double twinning*

$\{11\bar{2}2\}\rightarrow\{10\bar{1}2\}$ double twins are also characterized in rolled pure titanium at room temperature. We examined the selection of secondary twin variant according to the SF analysis, displacement gradient accommodation, and nucleation based on dislocation dissociation. Corresponding to the misorientation between secondary twins and the primary twin, six twin variants $\mathbf{T_i^I}$ are conventionally classified into 3 groups — Group I: $\mathbf{C_i^I}\rightarrow\mathbf{T_{i+3}^I}$ and $\mathbf{T_{i+4}^I}$, Group II: $\mathbf{C_i^I}\rightarrow\mathbf{T_i^I}$ and $\mathbf{T_{i+1}^I}$, and Group III: $\mathbf{C_i^I}\rightarrow\mathbf{T_{i+2}^I}$ and $\mathbf{T_{i+5}^I}$. Such classifications show the advantage regarding displacement gradient accommodation, two variants in the same group have the same contribution to displacement gradient accommodation. However, such classification is inconvenient to the discussion of the activity of secondary twins with respect to the SF. Twin variants $\mathbf{T_i^I}$ and $\mathbf{T_{i+3}^I}$ have the same SF, but they are categorized into Groups I and II, because experimental observations show a strong correlation of twin variant with the SF.

Fig. 11a shows an EBSD pattern where the contraction twin contains two secondary extension twins. The trace of the twinning plane associated with the contraction twin is nearly parallel to the horizontal axis. With the help of pole figures in Fig. 11b, a misorientation angle of the $(1\bar{2}12)$ twin plane between C_5^I twin and the matrix is 3.35°. Therefore, the contraction twin is determined to be twin variant C_5^I. In the pole figure of $\{10\bar{1}2\}$ planes (Fig. 11c), a misorientation angle between $(0\bar{1}12)$ planes in the T_5^I twin and in the matrix is 1.21°, and that between $(1\bar{1}02)$ planes in the T_6^I twin and in the matrix is 0.80°. Fig. 11d shows the pole figure of the corresponding twinning directions. The misorientation angle between $[01\bar{1}1]$ directions in the T_5^I twin and in the matrix is 1.22°, and that between $[\bar{1}101]$ directions in the T_6^I and in the matrix is 0.81°. According to the crystallography of twins $\{10\bar{1}2\}<\bar{1}011>$, the two secondary twin variants are twin variants T_5^I and T_6^I, belonging to Group II. We compared experiment result with the SF analysis. As shown in Fig. 11a, C_5^I is the primary contraction twin, T_5^I and T_6^I are secondary twin. The SFs associated with C_5^I,T_5^I and T_6^I are 0.4295, 0.3511 and 0.3927, respectively. The SF of T_6^I is larger than that of T_5^I and the difference between T_5^I and T_6^I is 0.041, which is smaller than 0.05. This is in agreement with our prediction. The loading direction identified for the grain according to the projection of external ND into the crystal frame is located at the predicted loading domain, as indicated by a black dot in Fig. 9e. This implies that the SF criterion is well satisfied. The displacement gradient accommodation and the nucleation of TDs based on dislocation dissociation are also satisfied.

Fig. 12a shows an EBSD pattern where the contraction twin contains one secondary extension twin variant. With the help of pole figures in Fig. 12b, the misorientation angle between $(11\bar{2}2)$ planes in the C_4^I twin and in the matrix is 0.85°. Therefore, C_4^I twin variant can be identified as the primary twin. In the pole figure of $\{10\bar{1}2\}$ planes (Fig. 12c), the misorientation angle between $(10\bar{1}2)$ planes in the T_4^I twin and in the matrix is 0.72°. The misorientation angle between $[\bar{1}011]$ directions in the T_4^I twin and in the matrix is

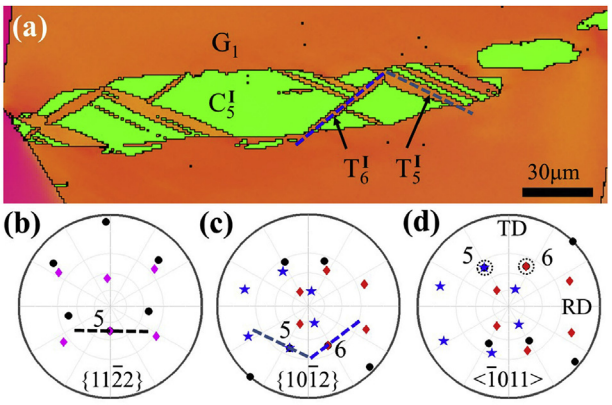

Fig. 11. (a) An EBSD map of two secondary $\{10\bar{1}2\}$ twins in a primary $\{11\bar{2}2\}$ contraction twin as well as pole figures of (b) $\{11\bar{2}2\}$ plane, (c) $\{10\bar{1}2\}$ plane, (d) $\bar{1}011$ direction. In (b), the black dots represent six $\{11\bar{2}2\}$ twin planes in the matrix, the pink diamonds represent six $\{11\bar{2}2\}$ in the twin. In (c), the black dots represent six $\{10\bar{1}2\}$ twin planes in the matrix, the red diamonds and blue stars represent six $\{10\bar{1}2\}$ twin planes in the two $\{10\bar{1}2\}$ twins, and (d) the black dots represent six $\bar{1}011$ twin directions in the matrix, the red diamonds and blue stars represent six $\bar{1}011$ twin directions in the twin. (For interpretation of the references to colour in this figure legend, the reader is referred to the web version of this article.)

0.73° as shown in Fig. 12d. T_4^I is thus the active twin variant, belonging to Group II. The same analysis was performed for the case in Fig. 12. We found that the SFs associated with C_4^I and T_4^I are 0.3222 and 0.473. The other twin variant T_5^I in Group II is 0.202, which is much smaller than T_4^I. This explains why it is unfavorable and only one twin variant appears, and T_4^I is activated. The loading direction identified for the grain according to the projection of external ND into the crystal frame is located at the predicted loading domain, as indicated by a blue dot in Fig. 9f, which shows the loading domain for C_4^I variant where the SF of C_4^I variant is greater than 0.3 and is the greatest among six equivalent variants. This result again demonstrates the SF criterion must be satisfied and predict the selection of twin variants. The displacement gradient accommodation and the nucleation of TDs based on dislocation dissociation are also satisfied, but can not predict the selection of the activated twin variant.

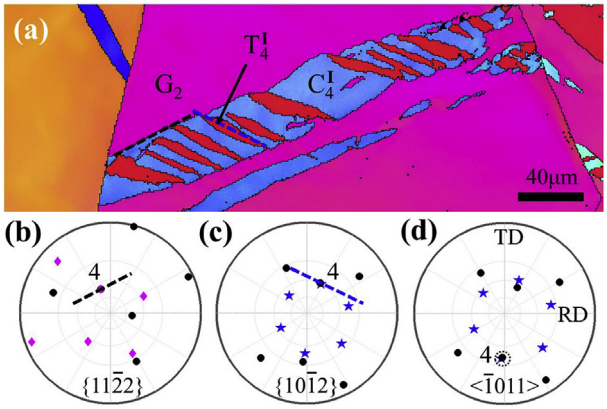

Fig. 12. (a) An EBSD map of one secondary $\{10\bar{1}2\}$ twin in a primary $\{11\bar{2}2\}$ contraction twin as well as pole figures of (b) $\{11\bar{2}2\}$ plane, (c) $\{10\bar{1}2\}$ plane, (d) $\bar{1}011$ direction. In (b), the black dots represent six $\{11\bar{2}2\}$ twin planes in the matrix, the pink diamonds represent six $\{11\bar{2}2\}$ in the twin. In (c), the black dots represent six $\{10\bar{1}2\}$ twin planes in the matrix, the blue stars represent six $\{10\bar{1}2\}$ twin planes in the $\{10\bar{1}2\}$ twin, and (d) the black dots represent six $\bar{1}011$ twin directions in the matrix, the blue stars represent six $\bar{1}011$ twin directions in the twin. (For interpretation of the references to colour in this figure legend, the reader is referred to the web version of this article.)

6. Conclusions

We experimentally studied sequential twinning in rolled pure titanium at room temperature, and identified a new sequential twinning mechanism $T^{II}_{i-1}T^{II}_{i} \rightarrow T^{I}_{i}$, i.e., $\{10\bar{1}2\}$ extension twin stimulated by the primary $\{11\bar{2}1\}$ twin-twin junction. The SF analysis as the local stress is taken into account is able to determine the position of sequential twin variant, but cannot determine the twin variant in the group of twin variants. Displacement gradient accommodation is further used to determine the twin variant.

The well-known secondary $\{10\bar{1}2\}$ extension twins in primary $\{11\bar{2}2\}$ contraction twins (referred to as $C^{I}_{i} \rightarrow T^{I}_{j}$ double twinning) are also analyzed according to our EBSD analysis. Experiment observations can be well accounted for according to the SF analysis. Displacement gradient accommodation and the nucleation of TDs based on dislocations dissociation only work well for the most active twin variants, but cannot address other phenomena associated with $C^{I}_{i} \rightarrow T^{I}_{j}$ double twinning. For example, the three criteria predict that Group II twins are predominant among three groups, in consistent with statistical analysis. However, the displacement gradient accommodation and the nucleation of TDs based on dislocation dissociation cannot predict the selection of the activated twin variant in Group II. Compared to them, The SF analysis is able to predict the activated twin variant. For activated twin variants in Group I and III, displacement gradient accommodation was not satisfied, showing the opposite trend.

Acknowledgements

S. Xu thanks the Ministry of National Education, Higher Education and Research of France for providing the Doctoral Contract. M.Y. Gong, X.Y. Xie and J. Wang acknowledge the support by the Nebraska Center for Energy Sciences Research, University of Nebraska-Lincoln. Jian Wang also acknowledges support from the US National Science Foundation (NSF) (CMMI-1661686).

References

[1] K. Amouzou, T. Richeton, A. Roth, M. Lebyodkin, T. Lebedkina, Micromechanical modeling of hardening mechanisms in commercially pure α-titanium in tensile condition, Int. J. Plast. 80 (2016) 222–240.
[2] O. Ozugwu, M. Wang, Titanium alloys and their machinability, J. Mater. Proc. Tech. 68 (1997) 262–274.
[3] C. Tomé, I. Beyerlein, J. Wang, R. McCabe, A multi-scale statistical study of twinning in magnesium, JOM 63 (2011) 19–23.
[4] J. Wang, I. Beyerlein, C. Tomé, An atomic and probabilistic perspective on twin nucleation in Mg, Scr. Mater 63 (2010) 741–746.
[5] C. Cepeda-Jiménez, J. Molina-Aldareguia, M. Pérez-Prado, Origin of the twinning to slip transition with grain size refinement, with decreasing strain rate and with increasing temperature in magnesium, Acta Mater 88 (2015) 232–244.
[6] L. Jiang, J.J. Jonas, R. Mishra, A. Luo, A. Sachdev, S. Godet, Twinning and texture development in two Mg alloys subjected to loading along three different strain paths, Acta Mater 55 (2007) 3899–3910.
[7] J. Del Valle, F. Carreño, O.A. Ruano, Influence of texture and grain size on work hardening and ductility in magnesium-based alloys processed by ECAP and rolling, Acta Mater 54 (2006) 4247–4259.
[8] H. Wang, P. Wu, J. Wang, Modeling inelastic behavior of magnesium alloys during cyclic loading–unloading, Int. J. Plast. 47 (2013) 49–64.
[9] L. Wu, S. Agnew, D. Brown, G. Stoica, B. Clausen, A. Jain, D. Fielden, P. Liaw, Internal stress relaxation and load redistribution during the twinning–detwinning-dominated cyclic deformation of a wrought magnesium alloy, ZK60A, Acta Mater 56 (2008) 3699–3707.
[10] G. Proust, C.N. Tomé, A. Jain, S.R. Agnew, Modeling the effect of twinning and detwinning during strain-path changes of magnesium alloy AZ31, Int. J. Plast. 25 (2009) 861–880.
[11] S. Agnew, M. Yoo, C. Tome, Application of texture simulation to understanding mechanical behavior of Mg and solid solution alloys containing Li or Y, Acta Mater 49 (2001) 4277–4289.
[12] T. Al-Samman, X. Li, Sheet texture modification in magnesium-based alloys by selective rare earth alloying, Mater Sci. Eng. A 528 (2011) 3809–3822.
[13] J. Bohlen, M.R. Nürnberg, J.W. Senn, D. Letzig, S.R. Agnew, The texture and anisotropy of magnesium–zinc–rare earth alloy sheets, Acta Mater 55 (2007) 2101–2112.
[14] C. Cepeda-Jiménez, J. Molina-Aldareguia, M. Pérez-Prado, Effect of grain size on slip activity in pure magnesium polycrystals, Acta Mater 84 (2015) 443–456.
[15] J.T. Wang, J.Q. Liu, J. Tao, Y.L. Su, X. Zhao, Effect of grain size on mechanical property of Mg–3Al–1Zn alloy, Scr. Mater 59 (2008) 63–66.
[16] J.R. Greer, J.T.M. De Hosson, Plasticity in small-sized metallic systems: intrinsic versus extrinsic size effect, Prog. Mater Sci. 56 (2011) 654–724.
[17] P. Partridge, The crystallography and deformation modes of hexagonal close-packed metals, Metall. Rev. 12 (1967) 169–194.
[18] M. Yoo, Slip, twinning, and fracture in hexagonal close-packed metals, Metall. Trans. A 12 (1981) 409–418.
[19] A.A. Salem, S.R. Kalidindi, R.D. Doherty, Strain hardening of titanium: role of deformation twinning, Acta Mater 51 (2003) 4225–4237.
[20] S. Xu, C. Schuman, J.-S. Lecomte, Accommodative twins at high angle grain boundaries in rolled pure titanium, Scr. Mater 116 (2016) 152–156.
[21] L. Capolungo, I. Beyerlein, Nucleation and stability of twins in hcp metals, Phys. Rev. B 78 (2008) 024117.
[22] S. Jin, K. Marthinsen, Y. Li, Formation of {11-21} twin boundaries in titanium by kinking mechanism through accumulative dislocation slip, Acta Mater 120 (2016) 403–414.
[23] N.J. Lane, S.I. Simak, A.S. Mikhaylushkin, I.A. Abrikosov, L. Hultman, M.W. Barsoum, First-principles study of dislocations in hcp metals through the investigation of the (11-21) twin boundary, Phys. Rev. B 84 (2011) 184101.
[24] L. Wang, R. Barabash, T. Bieler, W. Liu, P. Eisenlohr, Study of {11-21} twinning in α-Ti by EBSD and laue microdiffraction, Metall. Mater Trans. A 44 (2013) 3664–3674.
[25] S. Wang, Y. Zhang, C. Schuman, J.-S. Lecomte, X. Zhao, L. Zuo, M.-J. Philippe, C. Esling, Study of twinning/detwinning behaviors of Ti by interrupted in situ tensile tests, Acta Mater 82 (2015) 424–436.
[26] J. Wang, I. Beyerlein, J. Hirth, C. Tomé, Twinning dislocations on {-1011} and {-1013} planes in hexagonal close-packed crystals, Acta Mater 59 (2011) 3990–4001.
[27] J.W. Christian, S. Mahajan, Deformation twinning, Prog. Mater Sci. 39 (1995) 1–157.
[28] H. El Kadiri, C.D. Barrett, M.A. Tschopp, The candidacy of shuffle and shear during compound twinning in hexagonal close-packed structures, Acta Mater 61 (2013) 7646–7659.
[29] W. Tirry, S. Bouvier, N. Benmhenni, W. Hammami, A. Habraken, F. Coghe, D. Schryvers, L. Rabet, Twinning in pure Ti subjected to monotonic simple shear deformation, Mater Charact. 72 (2012) 24–36.
[30] Y. Wang, J. Huang, Texture analysis in hexagonal materials, Mater Chem. Phys. 81 (2003) 11–26.
[31] M. Al-Maharbi, I. Karaman, I.J. Beyerlein, D. Foley, K.T. Hartwig, L.J. Kecskes, S.N. Mathaudhu, Microstructure, crystallographic texture, and plastic anisotropy evolution in an Mg alloy during equal channel angular extrusion processing, Mater Sci. Eng. A 528 (2011) 7616–7627.
[32] Y. Xin, M. Wang, Z. Zeng, M. Nie, Q. Liu, Strengthening and toughening of magnesium alloy by {10-12} extension twins, Scr. Mater 66 (2012) 25–28.
[33] M. Knezevic, A. Levinson, R. Harris, R.K. Mishra, R.D. Doherty, S.R. Kalidindi, Deformation twinning in AZ31: influence on strain hardening and texture evolution, Acta Mater 58 (2010) 6230–6242.
[34] H. Wang, P. Wu, J. Wang, C. Tomé, A crystal plasticity model for hexagonal close packed (HCP) crystals including twinning and de-twinning mechanisms, Int. J. Plast. 49 (2013) 36–52.
[35] H. El Kadiri, J. Kapil, A. Oppedal, L. Hector, S.R. Agnew, M. Cherkaoui, S. Vogel, The effect of twin–twin interactions on the nucleation and propagation of twinning in magnesium, Acta Mater 61 (2013) 3549–3563.
[36] C. Xie, Q. Fang, X. Liu, P. Guo, J. Chen, M. Zhang, Y. Liu, B. Rolfe, L. Li, Theoretical study on the deformation twinning and cracking in coarse-grained magnesium alloys, Int. J. Plast. 82 (2016) 44–61.
[37] Q. Yu, J. Wang, Y. Jiang, R.J. McCabe, C.N. Tomé, Co-zone {-1012} twin interaction in magnesium single crystal, Mater Res. Lett. 2 (2014) 82–88.
[38] Q. Yu, J. Wang, Y. Jiang, R.J. McCabe, N. Li, C.N. Tomé, Twin–twin interactions in magnesium, Acta Mater 77 (2014) 28–42.
[39] X. Huang, K. Suzuki, A. Watazu, I. Shigematsu, N. Saito, Effects of thickness reduction per pass on microstructure and texture of Mg–3Al–1Zn alloy sheet processed by differential speed rolling, Scr. Mater 60 (2009) 964–967.
[40] W. Kim, S. Hong, Y. Kim, S. Min, H. Jeong, J. Lee, Texture development and its effect on mechanical properties of an AZ61 Mg alloy fabricated by equal channel angular pressing, Acta Mater 51 (2003) 3293–3307.
[41] W. Kim, J. Lee, W. Kim, H. Jeong, H. Jeong, Microstructure and mechanical properties of Mg–Al–Zn alloy sheets severely deformed by asymmetrical rolling, Scr. Mater 56 (2007) 309–312.
[42] W. Kim, S. Yoo, Z. Chen, H. Jeong, Grain size and texture control of Mg–3Al–1Zn alloy sheet using a combination of equal-channel angular rolling and high-speed-ratio differential speed-rolling processes, Scr. Mater 60 (2009) 897–900.
[43] J. Hirth, J. Wang, C. Tomé, Disconnections and other defects associated with twin interfaces, Prog. Mater Sci. 83 (2016) 417–471.
[44] X. Liao, J. Wang, J. Nie, Y. Jiang, P. Wu, Deformation twinning in hexagonal materials, MRS Bull. 41 (2016) 314–319.
[45] G. Proust, C. Tomé, G. Kaschner, Modeling texture, twinning and hardening evolution during deformation of hexagonal materials, Acta Mater 55 (2007)

2137–2148.
[46] H. Qiao, S. Agnew, P. Wu, Modeling twinning and detwinning behavior of Mg alloy ZK60A during monotonic and cyclic loading, Int. J. Plast. 65 (2015) 61–84.
[47] J. Wang, S. Yadav, J. Hirth, C. Tomé, I. Beyerlein, Pure-shuffle nucleation of deformation twins in hexagonal-close-packed metals, Mater Res. Lett. 1 (2013) 126–132.
[48] I. Beyerlein, R. McCabe, C. Tomé, Effect of microstructure on the nucleation of deformation twins in polycrystalline high-purity magnesium: a multi-scale modeling study, J. Mech. Phys. Solids 59 (2011) 988–1003.
[49] S. Godet, L. Jiang, A. Luo, J. Jonas, Use of Schmid factors to select extension twin variants in extruded magnesium alloy tubes, Scr. Mater 55 (2006) 1055–1058.
[50] C. Gu, L. Toth, M. Hoffman, Twinning effects in a polycrystalline magnesium alloy under cyclic deformation, Acta Mater 62 (2014) 212–224.
[51] J.J. Jonas, S. Mu, T. Al-Samman, G. Gottstein, L. Jiang, È. Martin. The role of strain accommodation during the variant selection of primary twins in magnesium, Acta Mater 59 (2011) 2046–2056.
[52] Z.-Z. Shi, Y. Zhang, F. Wagner, P.-A. Juan, S. Berbenni, L. Capolungo, J.-S. Lecomte, T. Richeton, On the selection of extension twin variants with low Schmid factors in a deformed Mg alloy, Acta Mater 83 (2015) 17–28.
[53] M.A. Kumar, I.J. Beyerlein, C.N. Tomé, Effect of local stress fields on twin characteristics in HCP metals, Acta Mater 116 (2016) 143–154.
[54] R. Lebensohn, C. Tomé, A study of the stress state associated with twin nucleation and propagation in anisotropic materials, Philos. Mag. A 67 (1993) 187–206.
[55] I. Beyerlein, C. Tomé, A probabilistic twin nucleation model for HCP polycrystalline metals, Proc. R. Soc. Lond. A Math. Phys. Eng. Sci. R. Soc. (2010) rspa20090661.
[56] T. Bieler, P. Eisenlohr, C. Zhang, H. Phukan, M. Crimp, Grain boundaries and interfaces in slip transfer, Curr. Opin. Solid State Mater. Sci. 18 (2014) 212–226.
[57] L. Capolungo, I. Beyerlein, C. Tomé, Slip-assisted twin growth in hexagonal close-packed metals, Scr. Mater 60 (2009) 32–35.
[58] L. Wang, Y. Yang, P. Eisenlohr, T. Bieler, M. Crimp, D. Mason, Twin nucleation by slip transfer across grain boundaries in commercial purity titanium, Metall. Mater Trans. A 41 (2010) 421–430.
[59] L. Wang, P. Eisenlohr, Y. Yang, T. Bieler, M. Crimp, Nucleation of paired twins at grain boundaries in titanium, Scr. Mater 63 (2010) 827–830.
[60] R. Xin, C. Guo, Z. Xu, G. Liu, X. Huang, Q. Liu, Characteristics of long {10-12} twin bands in sheet rolling of a magnesium alloy, Scr. Mater 74 (2014) 96–99.
[61] M. Arul Kumar, I.J. Beyerlein, R.J. McCabe, C.N. Tome, Grain neighbour effects on twin transmission in hexagonal close-packed materials, Nat. Commun. 7 (2016) 13826.
[62] H. Qin, J.J. Jonas, Variant selection during secondary and tertiary twinning in pure titanium, Acta Mater 75 (2014) 198–211.
[63] S. Wang, C. Schuman, L. Bao, J. Lecomte, Y. Zhang, J. Raulot, M. Philippe, X. Zhao, C. Esling, Variant selection criterion for twin variants in titanium alloys deformed by rolling, Acta Mater 60 (2012) 3912–3919.
[64] I. Beyerlein, J. Wang, M. Barnett, C. Tomé, Double twinning mechanisms in magnesium alloys via dissociation of lattice dislocations, Proc. R. Soc. A 468 (2012) p.1496–1520. The Royal Society.
[65] M. Barnett, Z. Keshavarz, A. Beer, X. Ma, Non-Schmid behaviour during secondary twinning in a polycrystalline magnesium alloy, Acta Mater 56 (2008) 5–15.
[66] J. Luo, A. Godfrey, W. Liu, Q. Liu, Twinning behavior of a strongly basal textured AZ31 Mg alloy during warm rolling, Acta Mater 60 (2012) 1986–1998.
[67] Q. Ma, H. El Kadiri, A. Oppedal, J. Baird, M. Horstemeyer, M. Cherkaoui, Twinning and double twinning upon compression of prismatic textures in an AM30 magnesium alloy, Scr. Mater 64 (2011) 813–816.
[68] É. Martin, L. Capolungo, L. Jiang, J.J. Jonas, Variant selection during secondary twinning in Mg–3% Al, Acta Mater 58 (2010) 3970–3983.
[69] A. Jäger, A. Ostapovets, P. Molnár, P. Lejček, {10-12}-{10-12} Double twinning in magnesium, Philos. Mag. Lett. 91 (2011) 537–544.
[70] J. Jain, J. Zou, C. Sinclair, W. Poole, Double tensile twinning in a Mg–8Al–0.5 Zn alloy, J. Microsc. 242 (2011) 26–36.
[71] Z.-Z. Shi, Y. Zhang, F. Wagner, T. Richeton, P.-A. Juan, J.-S. Lecomte, L. Capolungo, S. Berbenni, Sequential double extension twinning in a magnesium alloy: combined statistical and micromechanical analyses, Acta Mater 96 (2015) 333–343.
[72] N. Bozzolo, L. Chan, A.D. Rollett, Misorientations induced by deformation twinning in titanium, J. Appl. Crystallogr. 43 (2010) 596–602.
[73] M. Knezevic, M. Zecevic, I.J. Beyerlein, J.F. Bingert, R.J. McCabe, Strain rate and temperature effects on the selection of primary and secondary slip and twinning systems in HCP Zr, Acta Mater 88 (2015) 55–73.
[74] W. Tirry, M. Nixon, O. Cazacu, F. Coghe, L. Rabet, The importance of secondary and ternary twinning in compressed Ti, Scr. Mater 64 (2011) 840–843.
[75] S. Xu, L.S. Toth, C. Schuman, J.-S. Lecomte, M.R. Barnett, Dislocation mediated variant selection for secondary twinning in compression of pure titanium, Acta Mater 124 (2017) 59–70.
[76] B. Beausir, J.-J. Fundenberger, ATOM - Analysis Tools for Orientation Maps, Université de Lorraine - Metz, 2015. http://atom-software.eu/.
[77] E. Roberts, P. Partridge, The accommodation around {10-12}<-1011> twins in magnesium, Acta Metall. 14 (1966) 513–527.
[78] D. Tromans, Elastic anisotropy of HCP metal crystals and polycrystals, Int. J. Res. Rev. Appl. Sci. 6 (2011) 462–483.